

vides a quadrature phase for 2.4 GHz and an octal phase for 5.2 GHz to generate an IQ signal for the sub-harmonic mixer. Figure 3 shows the sub-harmonic mixer schematic [3]. This mixer can also be used as a traditional Gilbert mixer if LO_0 port is connected to LO_180 port; and the LO_90 port is connected to LO_270 port simultaneously. Therefore, the circuit design can be simplified. There is an additional function of this mixer, which is a band selector. Depending on the receiving RF signal strength, a band-selecting control signal coming from the baseband can be used to control the on/off of this mixer. Because of this mechanism, we can easily select which band we chose before the band-pass filter. A 10 MHz center frequency and 20 MHz bandwidth polyphase band-pass filter is designed to provide the image rejection and filtering out the unwanted high frequency signal. To save power consumption and chip area, gm-C cell is implemented for this polyphase band-pass filter.

3. MEASUREMENT RESULT

This concurrent compact dual-band receiver is implemented using HHNEC 0.18- μm CMOS 1P6M technology. For a 1.8 V power supply, the overall power consumptions is simulated to be 66.1 mW. Table 1 summarizes all the measurement results. The proposed dual-band receiver has a fairly good performance as compared with the conventional receivers of individual receiving paths (as shown in Table 2). For noise issue, differential design concept is introduced. In addition, we not only use double guard ring layout style (N-well and P-substrate) to surround each individual block, but also individual power supply is used for each block. Another layout consideration is the RF signal penetrating through substrate issue; therefore, a metal1-shielding layer is added to form an ideal ground plate. Figure 4 shows the die photo of the proposed RF front-end chip with a die size of $2450 \times 1700 \mu\text{m}^2$. Figure 5 shows the dual-band receiver and Figure 6 shows the measured results.

4. CONCLUSION

A low-cost and low-power IEEE 802.11a/b/g compact dual-band radio receiver for wireless LAN applications has been designed in a standard 0.18- μm CMOS 1P6M technology. To save chip area, sub-harmonic mixer is used so that only one multi-modulus synthesizer is needed for this compact dual-band receiver design. The receiver has a simulated 2.8 dB and 4.3 dB receiver chain noise figure at 2.45 GHz and 5.25 GHz, respectively. For a 1.8 V power supply, the overall power consumption was only 66.1 mW.

REFERENCES

1. B.-U. Klepser, M. Punzenberger, T. Ruhlicke, and M. Zannoth, 5-GHz and 2.4-GHz dual-band RF-transceiver for WLAN 802.11a/b/g applications, Proceedings of IEEE Radio Frequency Integrated Circuits (RFIC) Symposium, Philadelphia, PA 8–10 June 2003, pp. 37–40.
2. B. McFarland, A. Shor, and A. Tabatabaei, A 2.4 & 5 GHz dual band 802.11 WLAN supporting data rates to 108 Mb/s, Proceedings of Gallium Arsenide Integrated Circuit (GaAs IC) Symposium, 2002, 24th Annual Technical Digest, 20–23 October 2002, pp. 11–14.
3. M. Goldfarb, E. Balboni, and J. Cavey, Even harmonic double-balanced active mixer for use in direct conversion receivers, IEEE J Solid-State Circuits 38 (2003), 1762–1766.
4. A. Abidi, Direct-conversion radio transceivers for digital communications, IEEE J Solid-State Circuits 30 (1995), 1399–1410.
5. S.A. Sanielevici, K.R. Cioffi, B. Ahrari, P.S. Stephenson, D.L. Skoglund, and M. Zargari, A 900-MHz transceiver chipset for two-way paging applications, IEEE J Solid-State Circuits 33 (1998), 2160–2168.
6. K. Vavelidis, I. Vassiliou, T. Georgantas, A. Yamanaka, S. Kavadias, G. Kamoulakos, C. Kapnistis, Y. Kokolakis, A. Kyranas, P. Merakos, I. Bouras, S. Bouras, S. Plevridis, and N. Haralabidis, A Dual-Band

- 5.15–5.35-GHz, 2.4–2.5-GHz 0.18- μm CMOS Transceiver for 802.11a/b/g Wireless LAN, IEEE J Solid-State Circuits 39 (2004), 1180–1184.
7. Z. Markus, R. Thomas, and K. Bernd-Ulrich, TA highly integrated dual-band multimode wireless LAN transceiver, IEEE J Solid-State Circuits 39 (2004), 1191–1195.
8. 802.11a/b/g Chip Set, Product Brief, Agere systems, 2003.
9. 802.11a/b/g Dual-Band Wireless LAN Transceiver, Product Brief, Agere systems WL54040, 2003.
10. Wireless LAN IEEE 802.11a/b/g Chipset, Product Brief, RFMD, RFCS5420.
11. Z. Li, R. Quintal, and K.K. O, A dual-band CMOS front-end with two gain modes for wireless LAN applications, IEEE J Solid-State Circuits 39 (2004), 2069–2073.
12. H. Hashemi and A. Hajimiri, Concurrent multiband low-noise amplifiers-theory, design, and applications, IEEE J Solid-State Circuits 50 (2002), 288–301.

© 2009 Wiley Periodicals, Inc.

EFFICIENT TENSOR BASED FDTD SCHEME FOR MODELING SLOPED INTERFACES IN LOSSY MEDIA

Gurpreet Singh,¹ Eng Leong Tan,¹ and Zhi Ning Chen²

¹ School of Electrical and Electronic Engineering, Nanyang Technological University, Singapore 639798; Corresponding author: gurp0002@ntu.edu.sg

² Institute for Infocomm Research, Singapore

Received 5 October 2008

ABSTRACT: This article presents an efficient tensor based finite-difference time-domain (FDTD) scheme for modeling sloped interfaces in lossy media. The formulated scheme achieves its improved efficiency by implicitly solving the internal fields affected by an interface. This permits the reduction of updating coefficients in the scheme. FDTD simulations that are generally used to compute scattering parameters or radar cross sections gain from this implicit computation. The scheme is formulated without assuming any single frequency approximation, previously assumed in the literature. This permits FDTD simulation results over a wide frequency bandwidth in a single FDTD simulation run. To allow a more accurate and conformal approximation, the scheme extends the use of cell filling ratio to lossy media. © 2009 Wiley Periodicals, Inc. Microwave Opt Technol Lett 51: 1530–1537, 2009; Published online in Wiley InterScience (www.interscience.wiley.com). DOI 10.1002/mop.24398

Key words: finite-difference time-domain (FDTD) method; 2-dimension tensor; sloped interfaces; lossy media

1. INTRODUCTION

The finite-difference time-domain (FDTD) method has been widely used to obtain solutions of Maxwell's equations in complex geometries with complex materials. However, a significant flaw is its staircase approximation of planar, sloped or curved interfaces between different media on a Cartesian FDTD grid. Various methods [1, 2] have been proposed to minimize the errors caused by the staircase approximation. One such class of methods is based on properly constructing an average of the material's properties in the vicinity of the interface and using it to accurately solve the affected field components. For dielectrics, various effective permittivities have been determined in previous literature [2–5]. However, these permittivities do not completely account for the effective anisotropy induced by sloped or curved interface.

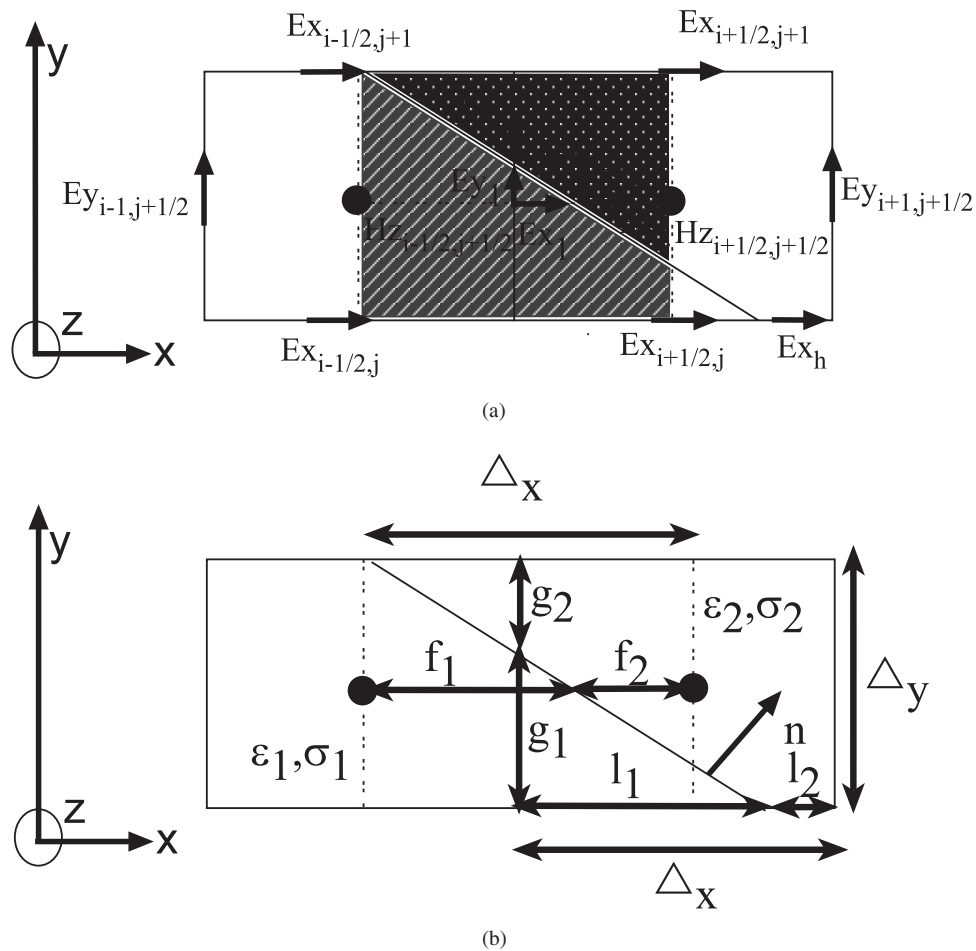


Figure 1 (a) Inhomogeneous FDTD cells. (b) Inhomogeneous FDTD cells

Recently, Nadobny et al. expanded on the method of Lee and Myung in [6], and proposed a tensor based FDTD formulation, referred to as tensor FDTD (TFDTD) to accurately treat the effective anisotropy induced by a sloped interface between lossless and lossy dielectric media [7, 8]. The TFDTD scheme was verified to achieve significantly improved numerical accuracy in comparison with analytical solutions. As a drawback, the TFDTD scheme, for the lossy media case, applies a single frequency approximation in its tensor derivation [8]. This restricts the FDTD simulation from achieving outputs with a wide frequency spectrum in one FDTD simulation run.

In this article, we further improve on the existing tensor based schemes in three ways. First, we formulate a tensor based FDTD scheme to implicitly solve the electric field components affected by an interface using auxiliary electric field components. This improves the computational efficiency by reducing the required number of updating coefficients and simplifies the magnetic field update equation. FDTD simulations that are generally used to compute scattering parameters or radar cross sections gain from the proposed scheme as such simulations do not explicitly require the internal electric field components that are affected by the interface. Second, we formulate the proposed scheme, without assuming any single frequency approximation, to allow accurate FDTD simulation results over a wide frequency bandwidth in one single FDTD simulation run. The single frequency approximation was assumed in the TFDTD scheme for lossy media [8]. Third, we extend the use of cell filling ratio into the proposed scheme to

permit a more accurate and conformal approximation. Cell filling ratio was previously introduced into tensor based schemes by Lee and Myung in [6] for lossless media. In Section 2, we derive the proposed tensor based FDTD scheme. In Section 3, we verify the numerical efficiency and accuracy of the proposed scheme with simulation results.

2. FORMULATIONS

2.1. Geometry

In this article, we develop FDTD update equations to approximate Maxwell's equation for the case of 2-D TE_z polarization. We assume that certain FDTD cells contain two different lossy mediums (denoted as medium 1 and 2 with permittivity/conductivity values of ϵ_1 / σ_1 and ϵ_2 / σ_2 , respectively) separated by a sloped interface with outward normal vector n , as shown in Figure 1. To derive an accurate FDTD scheme to solve the electric and magnetic field components affected by the sloped interface at grid points $(i, j + 1/2)$ and $(i + 1/2, j + 1/2)$, respectively, as shown in Figure 1(a), we need to rigorously perform the spatial and temporal approximation of Maxwell's equations at the respective grid points. In the derivation, we define the set of normalized dimension parameters, f_1/f_2 , g_1/g_2 , and l_1/l_2 , as shown in Figure 1(b). The electric field vector at every point in the slant-shaded region (medium 1) and dot-shaded region (medium 2) is assumed a constant vector field E_1 with components E_{x1} / E_{y1} and E_2 with components E_{x2} / E_{y2} , respectively. Note that the grid point $(i, j$

+ 1/2) lies in the slant-shaded region. The electric field component E_{xh} is assumed constant along the normalized dimension l_2 . These are illustrated in Figure 1(a). In the next Section, we introduce the auxiliary electric field vector E_c , that is used to implicitly solve E_1 at grid point $(i, j + 1/2)$. This improves the efficiency of the formulated scheme and simplifies the magnetic field update equation.

2.2. Approximation of Maxwell's Equations in the Integral Form

In this Section, we first derive the FDTD update equations to solve E_1 by performing the spatial approximation of Ampere's Law in the integral form,

$$\frac{\partial}{\partial t} \iint \mathbf{D} \cdot d\mathbf{s} = \oint \mathbf{H} \cdot d\mathbf{l} - \iint \mathbf{J} \cdot d\mathbf{s} \quad (1)$$

when $ds = ds\hat{x}$, yielding,

$$\frac{\partial}{\partial t} (\varepsilon_1 g_1 E_{x1} + \varepsilon_2 g_2 E_{x2}) = \frac{H_z|_{i,j+1} - H_z|_{i,j}}{\Delta_y} - (\sigma_1 g_1 E_{x1} + \sigma_2 g_2 E_{x2}) \quad (2)$$

and when $ds = ds\hat{y}$, yielding,

$$\frac{\partial}{\partial t} (\varepsilon_1 f_1 E_{y1} + \varepsilon_2 f_2 E_{y2}) = \frac{H_z|_{i-1/2,j+1/2} - H_z|_{i+1/2,j+1/2}}{\Delta_x} - (\sigma_1 f_1 E_{y1} + \sigma_2 f_2 E_{y2}) \quad (3)$$

Expressing Eqs. (2) and (3) in matrix form and performing the temporal approximation yields,

$$[a_1]E_1^{n+1/2} + [a_2]E_2^{n+1/2} = -[b_1]E_1^{n-1/2} + \left[\begin{array}{c} \frac{H_z|_{i,j+1} - H_z|_{i,j}}{\Delta_y} \\ \frac{H_z|_{i-1/2,j+1/2} - H_z|_{i+1/2,j+1/2}}{\Delta_x} \end{array} \right] - [b_2]E_2^{n-1/2} \quad (4)$$

where for $k = \{1,2\}$

$$[a_k] = \begin{bmatrix} \left(\frac{\sigma_k}{2} + \frac{\varepsilon_k}{\Delta_t}\right) g_k & 0 \\ 0 & \left(\frac{\sigma_k}{2} + \frac{\varepsilon_k}{\Delta_t}\right) f_k \end{bmatrix} \times [b_k] = \begin{bmatrix} \left(\frac{\sigma_k}{2} - \frac{\varepsilon_k}{\Delta_t}\right) g_k & 0 \\ 0 & \left(\frac{\sigma_k}{2} - \frac{\varepsilon_k}{\Delta_t}\right) f_k \end{bmatrix} \quad (5)$$

For the proposed scheme using cell filling ratios, the coefficients g_k and f_k , in matrix $[a_k]$ and $[b_k]$, are both replaced by a single coefficient c_k , with c_k representing the area (volume in 3-D) of medium k that is bounded by the edges of the FDTD cell centered at $(i, j + 1/2)$ and the sloped interface. Next, we derive the FDTD update equations to solve $H_z|_{i+1/2,j+1/2}$ by performing the spatial and temporal approximation of Faraday's Law in the integral form,

$$\frac{\partial}{\partial t} \iint \mathbf{B} \cdot d\mathbf{s} = -\oint \mathbf{E} \cdot d\mathbf{l} \quad (6)$$

when $ds = ds\hat{z}$, yielding,

$$H_z|_{i+1/2,j+1/2}^{n+1} = H_z|_{i+1/2,j+1/2}^n + (g_1 E_{y1}|^{n+1/2} + g_2 E_{y2}|^{n+1/2} - E_{y|_{i+1,j+1/2}}|^{n+1/2}) \frac{\Delta_t}{\mu_0 \Delta_x} + (E_{x1}|_{i+1/2,j+1}^{n+1/2} - l_1 E_{x1}|_{i+1/2,j}^{n+1/2} - l_2 E_{xh}|^{n+1/2}) \frac{\Delta_t}{\mu_0 \Delta_y} \quad (7)$$

2.3. Derivation of Auxiliary Vectors

In this Section, we introduce an auxiliary electric field vector E_c and derive explicit relations to replace the electric field vectors E_1 and E_2 in Eq. (4) and components in Eq. (7). First, let E_c at point $(i, j + 1/2)$ be related to E_1 and E_2 through the following equation in either time or Fourier domain,

$$E_c = \begin{bmatrix} f_1 & 0 \\ 0 & g_1 \end{bmatrix} E_1 + \begin{bmatrix} f_2 & 0 \\ 0 & g_2 \end{bmatrix} E_2 \quad (8)$$

A similar scalar relation to Eq. (8) was formed in [5]. Next, using the interface condition relation in Fourier domain,

$$E_2(\omega) = \begin{bmatrix} n_y^2 + n_x^2 \frac{\varepsilon_1(\omega)}{\varepsilon_2(\omega)} & \left(\frac{\varepsilon_1(\omega)}{\varepsilon_2(\omega)} - 1\right) n_y n_x \\ \left(\frac{\varepsilon_1(\omega)}{\varepsilon_2(\omega)} - 1\right) n_y n_x & n_x^2 + n_y^2 \frac{\varepsilon_1(\omega)}{\varepsilon_2(\omega)} \end{bmatrix} E_1(\omega) \quad (9)$$

where $\varepsilon_1(\omega) = \varepsilon_1 + \frac{\sigma_1}{j\omega}$ and $\varepsilon_2(\omega) = \varepsilon_2 + \frac{\sigma_2}{j\omega}$ and Eq. (8), E_1 and E_2 are each solved in terms of E_c ,

$$E_1(\omega) = Q(\omega) E_c(\omega) \quad E_2(\omega) = P(\omega) E_c(\omega) \quad (10)$$

where the elements of matrices $Q(\omega)$ and $P(\omega)$ are,

$$\begin{aligned} q_{11}(\omega) &= (\varepsilon_1(\omega) + (\varepsilon_2(\omega) - \varepsilon_1(\omega))(n_x^2 + g_1 n_y^2)) / \beta(\omega) \\ q_{12}(\omega) &= (\varepsilon_2(\omega) - \varepsilon_1(\omega))(f_2 n_x n_y) / \beta(\omega) \\ q_{21}(\omega) &= (\varepsilon_2(\omega) - \varepsilon_1(\omega))(g_2 n_x n_y) / \beta(\omega) \\ q_{22}(\omega) &= (\varepsilon_1(\omega) + (\varepsilon_2(\omega) - \varepsilon_1(\omega))(n_y^2 + f_1 n_x^2)) / \beta(\omega) \\ p_{11}(\omega) &= (\varepsilon_1(\omega) + (\varepsilon_2(\omega) - \varepsilon_1(\omega))(g_1 n_y^2)) / \beta(\omega) \\ p_{12}(\omega) &= (\varepsilon_1(\omega) - \varepsilon_2(\omega))(f_1 n_x n_y) / \beta(\omega) \\ p_{21}(\omega) &= (\varepsilon_1(\omega) - \varepsilon_2(\omega))(g_1 n_x n_y) / \beta(\omega) \\ p_{22}(\omega) &= (\varepsilon_1(\omega) + (\varepsilon_2(\omega) - \varepsilon_1(\omega))(f_1 n_x^2)) / \beta(\omega) \\ \beta(\omega) &= \varepsilon_1(\omega) + (\varepsilon_2(\omega) - \varepsilon_1(\omega))(f_1 n_x^2 + g_1 n_y^2) \end{aligned}$$

To inverse Fourier transform Eq. (10), the matrices $Q(\omega)$ and $P(\omega)$ are first split into the form,

$$\begin{aligned} Q(\omega) &= \frac{1}{\alpha + j\omega} [q_R] + \frac{j\omega}{\alpha + j\omega} [q_I] \\ P(\omega) &= \frac{1}{\alpha + j\omega} [p_R] + \frac{j\omega}{\alpha + j\omega} [p_I] \end{aligned} \quad (11)$$

where $[q_R]$, $[q_I]$, $[p_R]$, and $[p_I]$ are 2×2 real constant matrices. The inverse Fourier transform of Eq. (10) yields,

$$\begin{aligned}
\mathbf{E}_1(t) &= \mathbf{Q}(t) \otimes \mathbf{E}_c(t) \\
&= \left\{ [q_R]e^{-\alpha t}u(t) + [q_I] \frac{\partial}{\partial t}(e^{-\alpha t}u(t)) \right\} \otimes \mathbf{E}_c(t) \\
&= \{ ([q_R] - \alpha[q_I])e^{-\alpha t}u(t) + [q_I]\delta(t) \} \otimes \mathbf{E}_c(t) \\
&= ([q_R] - \alpha[q_I])e^{-\alpha t}u(t) \otimes \mathbf{E}_c(t) + [q_I]\mathbf{E}_c(t) \quad (12)
\end{aligned}$$

where \otimes represents the continuous-time convolution operator. Expressing Eq. (12) in discrete-time form yields,

$$\mathbf{E}_1|^{n+1/2} = (\Delta_t[q_R] - \Delta_t\alpha[q_I]) \sum_{m=0}^n e^{-\alpha(n-m)\Delta_t} \mathbf{E}_c|^{m+1/2} + [q_I]\mathbf{E}_c|^{n+1/2} \quad (13)$$

We introduce the vector \mathbf{I}_c and equate it to the summation term as,

$$\mathbf{I}_c|^{n+1/2} = \sum_{m=0}^n e^{-\alpha(n-m)\Delta_t} \mathbf{E}_c|^{m+1/2} \quad (14)$$

Expressing Eq. (14) in terms of an update equation yields,

$$\mathbf{I}_c|^{n+1/2} = \mathbf{E}_c|^{n+1/2} + \mathbf{I}_c|^{n-1/2}e^{-\alpha\Delta_t} \quad (15)$$

Finally, from Eqs. (13) and (14), the discrete-time forms of Eqs. (10) are expressed as,

$$\begin{aligned}
\mathbf{E}_1|^{n+1/2} &= (\Delta_t[q_R] - \Delta_t\alpha[q_I])\mathbf{I}_c|^{n+1/2} + [q_I]\mathbf{E}_c|^{n+1/2} \\
\mathbf{E}_2|^{n+1/2} &= (\Delta_t[p_R] - \Delta_t\alpha[p_I])\mathbf{I}_c|^{n+1/2} + [p_I]\mathbf{E}_c|^{n+1/2} \quad (16)
\end{aligned}$$

with Eq. (15) used to update vector $\mathbf{I}_c|^{n+1/2}$.

2.4. Efficient Tensor Based FDTD Scheme

Substituting Eqs. (15) and (16) into (4) yields the FDTD update equation to solve the auxiliary electric field vector \mathbf{E}_c at the grid point $(i, j + 1/2)$,

$$\begin{aligned}
\mathbf{E}_c|^{n+1/2} &= [\mathbf{S}]^{-1}[\mathbf{U}]\mathbf{E}_c|^{n-1/2} + [\mathbf{S}]^{-1}[\mathbf{T}]\mathbf{I}_c|^{n-1/2} \\
&+ [\mathbf{S}]^{-1} \left[\begin{array}{c} \frac{H_z|_{i,j+1}^n - H_z|_{i,j}^n}{\Delta_y} \\ H_z|_{i-1/2,j+1/2}^n - H_z|_{i+1/2,j+1/2}^n \\ \Delta_x \end{array} \right] \quad (17)
\end{aligned}$$

with equation

$$\mathbf{I}_c|^{n+1/2} = \mathbf{E}_c|^{n+1/2} + \mathbf{I}_c|^{n-1/2}e^{-\alpha\Delta_t}$$

used to update vector $\mathbf{I}_c|^{n+1/2}$. The updating coefficients in matrix form in Eq. (17) are given as,

$$\begin{aligned}
[\mathbf{S}] &= [a_1](\Delta_t([q_R] - \alpha[q_I]) + [q_I]) + [a_2](\Delta_t([p_R] - \alpha[p_I]) + [p_I]) \\
[\mathbf{T}] &= \Delta_t(-[b_1] - e^{-\alpha\Delta_t}[a_1])([q_R] - \alpha[q_I]) + \Delta_t(-[b_2] \\
&\quad - e^{-\alpha\Delta_t}[a_2])([p_R] - \alpha[p_I]) \\
[\mathbf{U}] &= -[b_1][q_I] - [b_2][p_I] \quad (18)
\end{aligned}$$

Equation (17) can be extended to update, in general, both the x and y component of vector \mathbf{E}_c at every FDTD grid point. However, similar to the conventional FDTD update equations [9], we need only solve for one field component at every FDTD grid point. As such, the two scalar update equations at general x and y polarized field component grid points are,

$$\begin{aligned}
E_{xc}|_{i+1/2,j}^{n+1/2} &= v_{11}E_{xc}|_{i+1/2,j}^{n-1/2} + v_{12}E_{yc}|_{i+1/2,j}^{n-1/2} \\
&+ \frac{s_{22}}{\delta_s} \left(\frac{H_z|_{i+1/2,j+1/2}^n - H_z|_{i+1/2,j-1/2}^n}{\Delta_y} \right) + w_{11}I_{xc}|_{i+1/2,j}^{n-1/2} \\
&\quad - \frac{s_{12}}{\delta_s} \left(\frac{H_z|_{i,j}^n - H_z|_{i+1,j}^n}{\Delta_x} \right) + w_{12}I_{yc}|_{i+1/2,j}^{n-1/2} \quad (19)
\end{aligned}$$

with $I_{xc}|_{i+1/2,j}^{n+1/2} = E_{xc}|_{i+1/2,j}^{n+1/2} + I_{xc}|_{i+1/2,j}^{n-1/2}e^{-\alpha\Delta_t}$ and

$$\begin{aligned}
E_{yc}|_{i,j+1/2}^{n+1/2} &= v_{21}E_{xc}|_{i,j+1/2}^{n-1/2} + v_{22}E_{yc}|_{i,j+1/2}^{n-1/2} \\
&\quad - \frac{s_{21}}{\delta_s} \left(\frac{H_z|_{i,j+1}^n - H_z|_{i,j}^n}{\Delta_y} \right) + w_{21}I_{xc}|_{i,j+1/2}^{n-1/2} \\
&\quad + \frac{s_{11}}{\delta_s} \left(\frac{H_z|_{i-1/2,j+1/2}^n - H_z|_{i+1/2,j+1/2}^n}{\Delta_x} \right) + w_{22}I_{yc}|_{i,j+1/2}^{n-1/2} \quad (20)
\end{aligned}$$

with $I_{yc}|_{i,j+1/2}^{n+1/2} = E_{yc}|_{i,j+1/2}^{n+1/2} + I_{yc}|_{i,j+1/2}^{n-1/2}e^{-\alpha\Delta_t}$

The updating coefficients v_{kl} , w_{kl} and s_{kl} are the elements of matrices $[\mathbf{S}]^{-1}[\mathbf{U}]$, $[\mathbf{S}]^{-1}[\mathbf{T}]$, and $[\mathbf{S}]$, respectively, and δ_s is the determinant of matrix $[\mathbf{S}]$. These updating coefficients together with α are computed at every electric field component grid point, respectively. Notice that if the off-diagonal updating coefficients (v_{21} , s_{21} , and w_{21}) in Eq. (20) do not reduce to zero, the updating of field component $E_{yc}|_{i,j+1/2}^{n+1/2}$ then depends on field components that are not directly available from the FDTD grid. These components are then attained by interpolation from four values in the neighboring grid points. As an example, $E_{xc}|_{i,j+1/2}^{n-1/2}$ in Eq. (20) is attained by,

$$E_{xc}|_{i,j+1/2}^{n-1/2} = \frac{1}{4} (E_{xc}|_{i+1/2,j}^{n-1/2} + E_{xc}|_{i-1/2,j}^{n-1/2} + E_{xc}|_{i+1/2,j+1}^{n-1/2} + E_{xc}|_{i-1/2,j+1}^{n-1/2}) \quad (21)$$

Similar type of interpolations were performed in [1, 7, 10]. Substituting Eqs. (8) into (7) yields the update equation to solve for the $H_z|_{i+1/2,j+1/2}^{n+1}$,

$$\begin{aligned}
H_z|_{i+1/2,j+1/2}^{n+1} &= H_z|_{i+1/2,j+1/2}^n + \frac{\Delta_t}{\mu_0\Delta_x} (E_{yc}|_{i,j+1/2}^{n+1/2} - E_{yl}|_{i+1,j+1/2}^{n+1/2}) \\
&\quad + \frac{\Delta_t}{\mu_0\Delta_y} (E_{xl}|_{i+1/2,j+1}^{n+1/2} - E_{xc}|_{i+1/2,j}^{n+1/2}) \quad (22)
\end{aligned}$$

Scalar expressions similar to (22) can solve for every other magnetic field component. Note that the originally intended electric field component $E_{y1}|^{n+1/2}$ affected by the interface is generally not equivalent to the auxiliary electric field component $E_{yc}|_{i,j+1/2}^{n+1/2}$. $E_{y1}|^{n+1/2}$ can be explicitly retrieved from Eq. (16). However, in most cases, the explicit retrieval of the internal field $E_{y1}|^{n+1/2}$ is not needed in FDTD simulations that generally compute scattering parameters or radar cross sections. For such FDTD simulations, the implicit computation of $E_{y1}|^{n+1/2}$ using $E_{yc}|_{i,j+1/2}^{n+1/2}$ is more efficient. This is verified in Section 3. Furthermore, notice the simplicity of the magnetic field update Eq. (22)

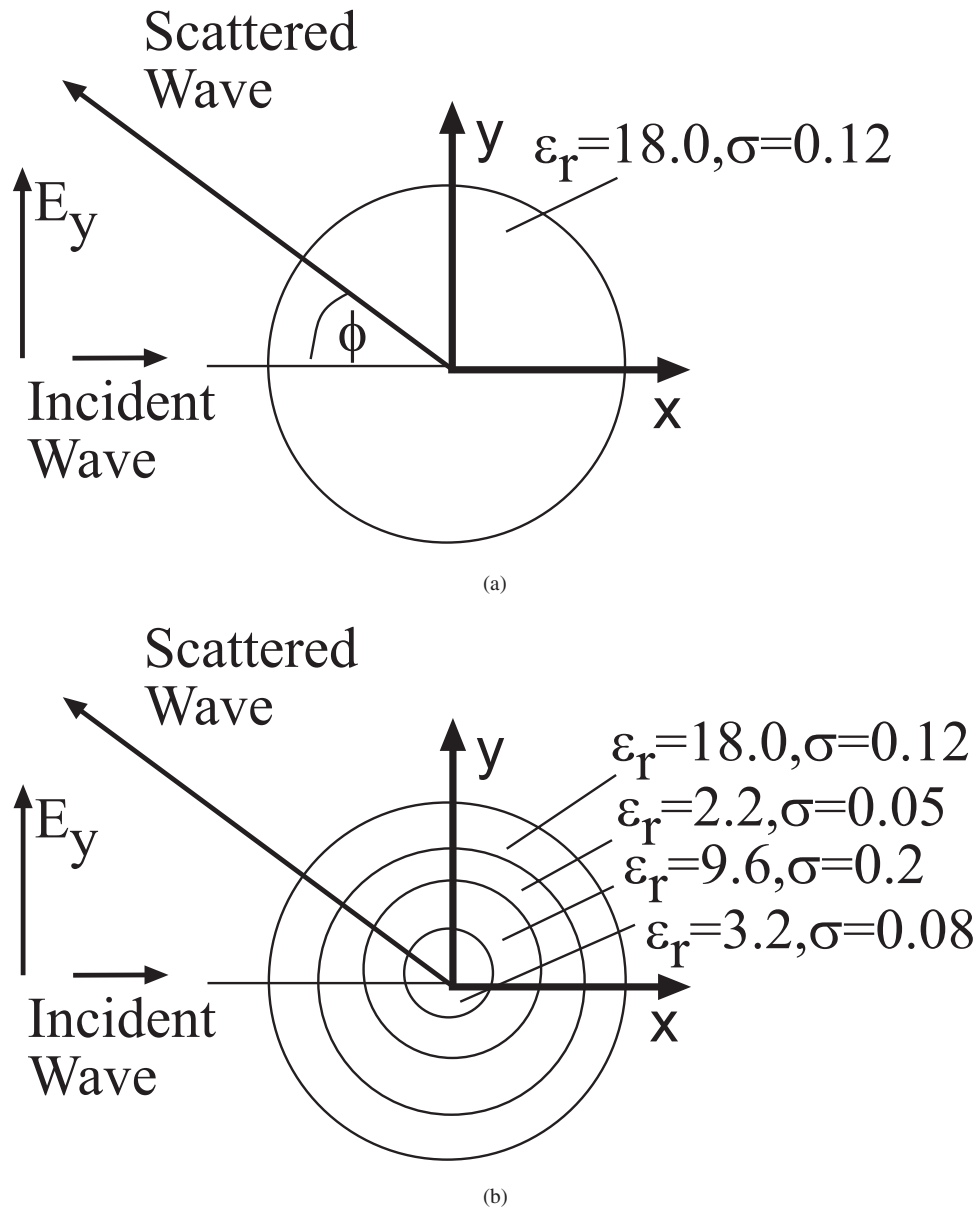


Figure 2 (a) Geometry of single layered circular lossy dielectric cylinder. (b) Geometry of four-layered circular lossy dielectric cylinder

in comparison to Eq. (7). Unlike Eq. (7), the updating coefficients in (22) do not require any preprocessing.

2.5. Special Cases

In this Section, we verify that the set of FDTD update equations from Eqs. (17), (18), and (22), under certain geometrical and material conditions, reduces to two known FDTD schemes in the literature.

2.5.1. Lossy and Electrically Homogeneous Regions By setting the geometrical parameters $f_1 = g_1 = 0$ and $f_2 = g_2 = 1$ and the complex permittivity $\epsilon_1(\omega) = \epsilon_2(\omega)$, the update Equation in (17) reduces to

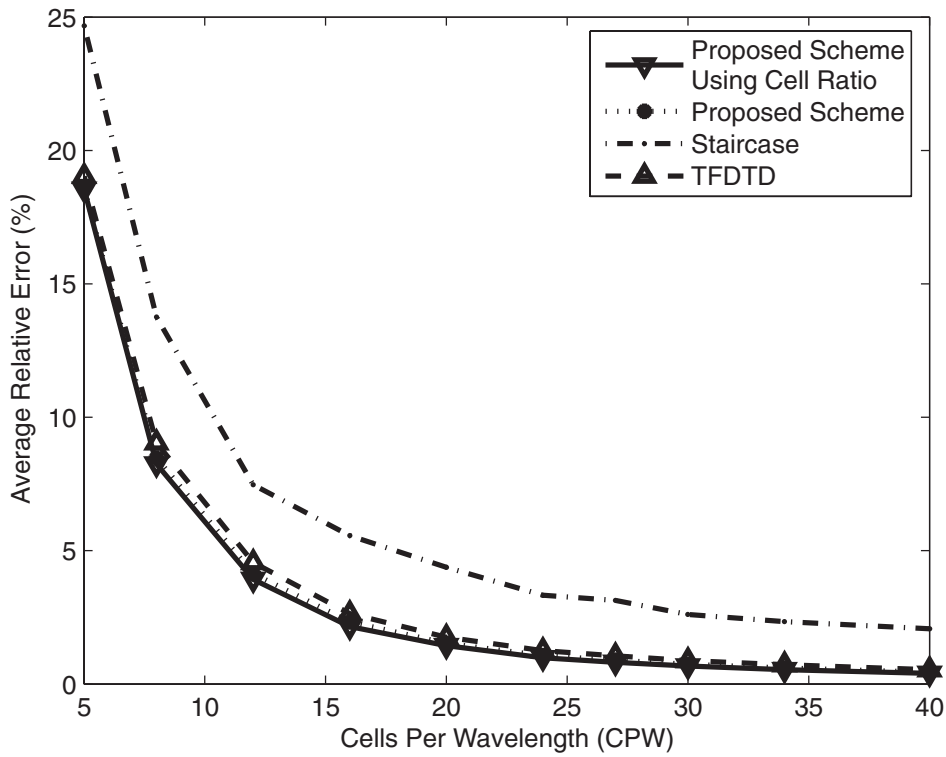
$$E_c^{n+1/2} = \begin{bmatrix} 2\epsilon_2 - \Delta_t\sigma_2 & 0 \\ 2\epsilon_2 + \Delta_t\sigma_2 & 0 \\ 0 & 2\epsilon_2 - \Delta_t\sigma_2 \\ 0 & 2\epsilon_2 + \Delta_t\sigma_2 \end{bmatrix} E_c^{n-1/2} +$$

$$\begin{bmatrix} \frac{2\Delta_t}{2\epsilon_2 + \Delta_t\sigma_2} & 0 \\ 0 & \frac{2\Delta_t}{2\epsilon_2 + \Delta_t\sigma_2} \end{bmatrix} \begin{bmatrix} \frac{H_{z|i,j+1}^n - H_{z|i,j}^n}{\Delta_y} \\ \frac{H_{z|i-1/2,j+1/2}^n - H_{z|i+1/2,j+1/2}^n}{\Delta_x} \end{bmatrix} \quad (23)$$

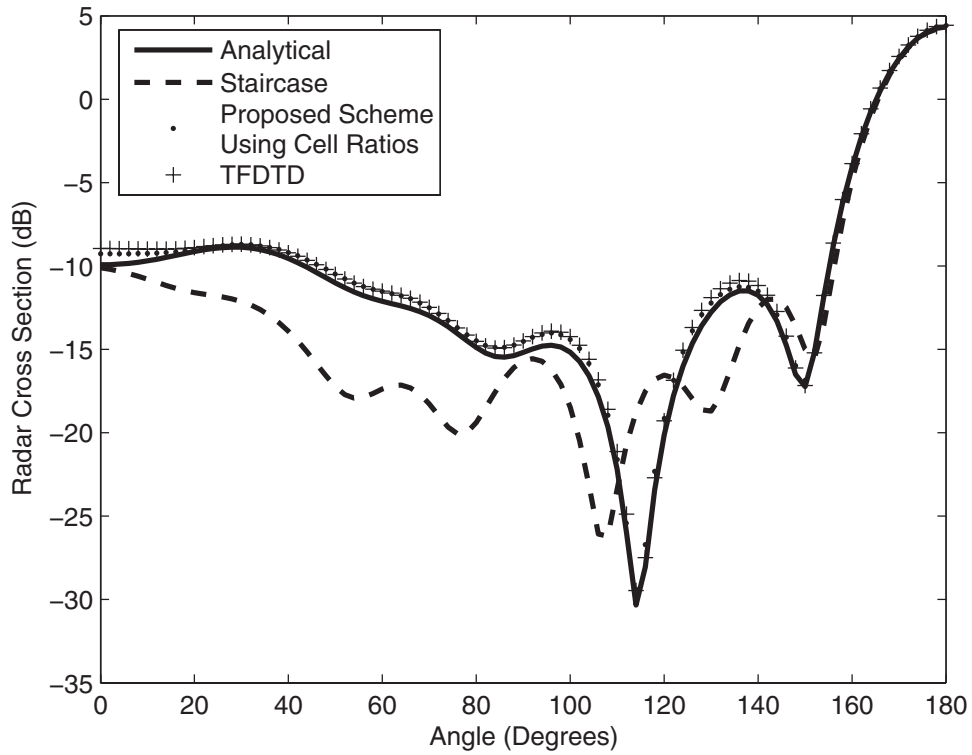
Substitution of $f_1 = g_1 = 0$ and $f_2 = g_2 = 1$ into Eq. (8) further yields,

$$E_c^{n+1/2} = E_2^{n+1/2}$$

Equation (23) is exactly the conventional FDTD update equation in an isotropic, homogeneous and lossy media [9]. Furthermore, the auxiliary electric field vector reduces to the original electric field vector in the homogeneous region and as such, the original field variables in Eq. (22) that are not affected by the interface ($E_y^{n+1/2}|_{i+1,j+1/2}$ and $E_x^{n+1/2}|_{i+1/2,j+1}$), can be replaced by the equivalent auxiliary field variables. In summary, once the geometrical and



(a)



(b)

Figure 3 (a) Radar cross section (RCS) result for single layered circular lossy dielectric cylinder. (b) Radar cross section (RCS) result for four-layered circular lossy dielectric cylinder

material parameters have been extracted from every electric field component grid point and the matrix coefficients in (18) have been preprocessed, one only needs to use Eqs. (19), (20), and (22), to solve for the fields in the entire FDTD computational domain.

2.5.2. Lossless and Electrically Inhomogeneous Regions Separated by Planar Interface. We assume that the sloped interface in Figure 1 is perpendicular to the electric field component E_{yc} at grid point $(i, j + 1/2)$. The geometrical parameters g_1 and g_2 are not

assumed to reduce to either 0 or 1 and $f_1 = 1$ and $f_2 = 0$. The two mediums are considered lossless with $\epsilon_1 \neq \epsilon_2$. The update equation in (17) then reduces to,

$$E_c|^{n+1/2} = E_c|^{n-1/2} + \begin{bmatrix} \frac{\Delta_t}{\epsilon_1 g_1 + \epsilon_2 g_2} & 0 \\ 0 & \frac{\Delta_t(\epsilon_1 g_2 + \epsilon_2 g_1)}{\epsilon_1 \epsilon_2} \end{bmatrix} \times \begin{bmatrix} \frac{H_{z|i,j+1}^n - H_{z|i,j}^n}{\Delta_y} \\ \frac{H_{z|i-1/2,j+1/2}^n - H_{z|i+1/2,j+1/2}^n}{\Delta_x} \end{bmatrix} \quad (24)$$

From Eq. (24), we observe that the first and second diagonal elements of the coefficient matrix are reduced and related to the weighted arithmetic and harmonic averaged effective permittivities [3, 5] when an electric field component is parallel and perpendicular, respectively, to the interface.

3. NUMERICAL EXPERIMENT

In this Section we validate the accuracy and efficiency of the FDTD update Eq. (19), (20), and (22), with and without cell filling ratios.

3.1. Numerical Accuracy

To validate the accuracy, we performed an experiment that numerically computed the bistatic radar cross section (RCS) of a plane wave illumination on an infinite single and four layered circular lossy dielectric cylinder of radius 10 cm. In the experiment, we varied the number of cells per wavelength (CPW), measured the relative RCS error given by,

$$\sqrt{\frac{\sum_{\phi} (\text{RCS}_{\text{FDTD}} - \text{RCS}_{\text{Analytic}})^2}{\sum_{\phi} \text{RCS}_{\text{Analytic}}^2}} \quad (25)$$

at every predefined frequency sampled at intervals of 0.1GHz within a 2GHz bandwidth. These relative RCS errors are then averaged over the entire bandwidth. The CPW was determined by computing the number of divisions for the shortest wavelength, for a given cell size. The plane wave was modeled using a bandpass Gaussian pulse with centre frequency of 2GHz, polarized in the y direction and propagating in the x direction in a background medium of air, $\epsilon_r = 1$. The geometrical and material parameters used in the two experiments are shown in Figure 2. Total field/scattered field formulation in a FDTD grid and perfectly matched layer with eight cells was applied. The experiment results were compared with analytical Bessel function solutions [11], with those calculated in the FDTD method using staircase approximation and the TFDTD scheme for lossy media [1]. For the single layered lossy cylinder, we present the results of average relative RCS error versus CPW, as shown in Figure 3(a) and for the four layered lossy cylinder, we present the results of radar cross section (RCS) measured at frequency of 3GHz and CPW = 16 versus angle ϕ , as shown in Figure 3(b).

From the results in Figure 3(a), we make some observations. First, the tensor based schemes, in general, reduces the average relative RCS error incurred when the staircase approximation was used, by an approximate value of 3 times at CPW = 20. Second, the tensor based schemes, in general, allows for the average relative RCS error to converge at a much lower value of about 0.5% at CPW = 40, compared to the allowed value of about 2%

by the staircase approximation. Third, to achieve the allowed convergence value of 2% by the staircase approximation, one needs to only use approximately 15 CPW in the proposed scheme, compared to 40 CPW, thereby improving the memory and simulation time performance. Fourth, the proposed scheme (with and without cell filling ratio) reduces the average relative RCS error incurred when the TFDTD scheme was used, by an approximate value of 1.2 times at CPW = 20. Hence, this verifies that the proposed scheme (with and without cell filling ratio) maintains the numerical accuracy of the TFDTD scheme. Fifth, the proposed scheme using cell filling ratio produces the lowest average relative RCS error across all CPW values and hence permits a more conformal approach. From the results in Figure 3(b), we observe that the tensor based schemes, in general, has better agreement with the analytical results. Furthermore, the proposed scheme has close agreement with the TFDTD scheme.

3.2. Computational Efficiency

To validate the computational efficiency, the number of preprocessed updating coefficients needed in the TFDTD scheme was compared to those needed in the proposed scheme. For the TFDTD scheme, we considered the update of a D_x and H_z field component that are affected by an interface, at the $n + 1/2$ and $n + 1$ time step, respectively. For the proposed scheme, we considered the update of E_{xc} and H_z field component [using Eqs. (19) and (22)] that are affected by an interface, at the $n + 1/2$ and $n + 1$ time step, respectively. The total number of updating coefficients reduces from a value of 16 in the TFDTD scheme to a value of 7 in the proposed scheme, thereby improving the computational efficiency. Furthermore, the proposed scheme was able to accurately solve for RCS values at 21 different frequencies, over a 2GHz bandwidth, in a single FDTD simulation run time compared to the 21 FDTD simulation run times needed by the TFDTD scheme with single frequency approximation.

4. CONCLUSION

This article has formulated an efficient tensor based FDTD scheme for modeling sloped interfaces in lossy media. The formulated scheme achieved its improved efficiency by implicitly solving the internal fields near the interface. This permitted the reduction of updating coefficients in the scheme. FDTD simulations that are generally used to compute scattering parameters or radar cross sections gain from this implicit computation. The formulated scheme was able to output numerically accurate results over a wide frequency bandwidth in a single FDTD simulation run, previously not possible in the TFDTD scheme because of the single frequency approximation. The proposed scheme extended the use of cell filling ratio into the tensor based scheme for lossy media and verified it as a more conformal approach. In future, we aim to extend the proposed tensor based FDTD scheme into unconditionally stable implicit finite-difference time-domain methods [12].

REFERENCES

1. T.G. Jurgens and A. Taflove, Three-dimensional contour FDTD modeling of scattering from single and multiple bodies, *IEEE Trans Antennas Propag* 41 (1993), 1703–1708.
2. S. Dev and R. Mittra, A conformal finite-difference time-domain technique for modeling cylindrical dielectric resonators, *IEEE Trans Microwave Theory Techn* 47 (1999), 1737–1739.
3. A. Mohammadi, H. Nadgaran, and M. Agio, Contour-path effective permittivities for the two-dimensional finite-difference time-domain method, *Opt Express* (2005), 10367–10381.
4. N. Kaneda, B. Houshmand, and T. Itoh, FDTD analysis of dielectric

resonators with curved surfaces, *IEEE Trans Antennas Propag* 45 (1997), 1645–1649.

5. K.P. Hwang and A.C. Cangellaris, Effective permittivities for second-order accurate FDTD equations at dielectric interfaces, *IEEE Microwave Wireless Comp Lett* 11 (2001), 158–160.
6. J.Y. Lee and N.H. Myung, Locally tensor conformal FDTD method for modeling arbitrary dielectric surfaces, *Microwave Opt Technol Lett* (1999), 245–249.
7. J. Nadobny, D. Sullivan, W. Wlodarczyk, P. Deuffhard, and P. Wust, A 3-D tensor FDTD-formulation for treatment of sloped interfaces in electrically inhomogeneous media, *IEEE Trans Antennas Propag* 51 (2003), 1760–1770.
8. J. Nadobny, D. Sullivan, and P. Wust, A general three-dimensional tensor FDTD-formulation for electrically inhomogeneous lossy media using the Z-transform, *IEEE Trans Antennas Propag* 56 (2008), 1027–1040.
9. A. Taflove and S.C. Hagness, *Computational electrodynamics: The finite-difference time-domain method*, Artech House, Boston, MA, 2005.
10. J. Schneider and S. Hudson, The finite-difference time-domain method applied to anisotropic material, *IEEE Trans Antennas Propag* 41 (1993), 994–999.
11. G.T. Ruck, *Radar cross section handbook*, Plenum Press, 1970.
12. E.L. Tan, Fundamental schemes for efficient unconditionally stable implicit finite-difference time-domain methods, *IEEE Trans Antennas Propag* 56 (2008), 170–177.

© 2009 Wiley Periodicals, Inc.

BROADBAND ARRAY ANTENNA WITH MARCHAND BALUN FOR 5.8 GHz BAND NOTCHED UWB APPLICATION

Q. Ma, B.-H. Sun, J.-F. Li, and Q.-Z. Liu

National Key Laboratory of Antennas and Microwave Technology, Xidian University, Xi'an, Shaanxi 710071, People's Republic of China; Corresponding author: maqingking@126.com

Received 17 September 2008

ABSTRACT: A two-element ultra wideband array antenna with a 5.8 GHz band-notch function is proposed. A novel Marchand balun feeding structure is chosen for its great merit of the equi-amplitude and 180° phase difference signals, making the omni-directional of radiation pattern much better. A simple u-shape slot is inserted into the radiating patch to create a frequency band-stop characteristic. The measured VSWR less than 2 is from 3.1 to 10.6 GHz, and the frequency notch band is from 5.7 to 5.9 GHz. The measured results agree well with the simulated. © 2009 Wiley Periodicals, Inc. *Microwave Opt Technol Lett* 51: 1537–1539, 2009; Published online in Wiley InterScience (www.interscience.wiley.com). DOI 10.1002/mop.24384

Key words: UWB; Marchand balun; broadband array

1. INTRODUCTION

Ultra wideband (UWB) systems have expanded rapidly in recent years, since Federal Communications Commission (FCC) allocated the frequency band of 3.1 to 10.6 GHz for the operation of devices in the new communication technology [1, 2]. However, within this UWB band, there are existing bands used by wireless local-area network (WLAN) operating in 5.8 GHz (5725–5825 MHz) band. It is necessary to design the UWB antenna with a notched band to minimize the interferences. Some reports on UWB antennas with band notched characteristics have been published [3–6]. Most of these antennas are monopole, which has low gain.

The array antennas can provide higher gains, but there are few references concerned to UWB array antennas.

In this article, we propose a two-element UWB array antenna using rectangle patch elements with a band-notch function for the UWB application. A Marchand balun [7] is used for the feeding, which feeds equi-amplitude and 180° phase difference signals to two output ports, the 180° phase difference makes improvements in pattern performance, and the broadband characteristics can be used in the UWB application. The feeding structure and the two radiation elements are coplane, and the Marchand balun is micro-strip feed, it makes the array antenna compact and small, the whole size of the array antenna is only $57 \times 26 \text{ mm}^2$, which is smaller than the antenna reported in the literature [8]. The array antenna without slot can cover the entire UWB frequency band and have a notch band for the 5.8 GHz frequency band by inserting slots into the elements. The VSWR and far-field radiation patterns of this antenna are analyzed and measured.

2. ANTENNA DESIGN

The geometry of the proposed band-notch array antenna is shown in Figure 1(a). A u-slot was added to reject the undesired frequency bandwidth. The array antenna is fabricated on a substrate with a thickness of $h = 1 \text{ mm}$, a dielectric constant of $\epsilon_r = 2.2$,

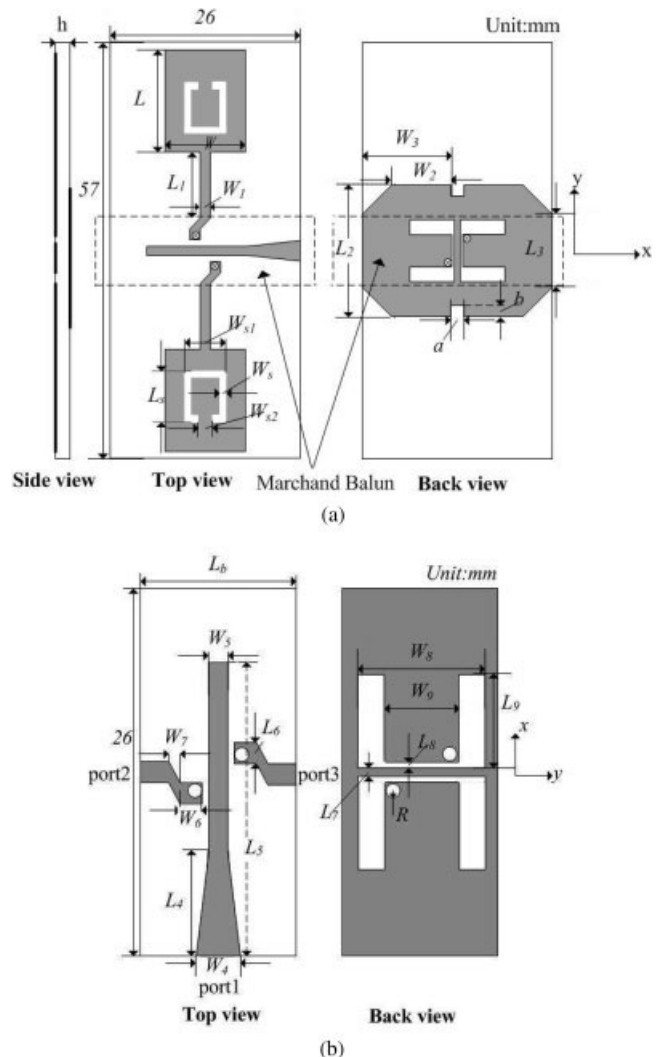


Figure 1 (a) The geometry of the integrated antenna with thickness $h = 1 \text{ mm}$. (b) The geometry of the Marchand balun